PHYSICAL REVIEW MATERIALS **7**, 065201 (2023)

Electronic excitations in monoclinic hafnia as studied by spatially and momentum-resolved electron energy-loss spectroscopy and *ab initio* density functional theory calculations

Sz-Chian Liou,[1,*] Guo-Jiun Shu,[2,3,†] Vladimir P. Oleshko,[4] Hwanhui Yun,[5]
Xiang-Lin Huang,[3] Hsin-An Chen,[2,6] and Wei-Tin Chen[7]
[1]*Electron Microscopy Facility, Institute for Functional Materials and Devices, Lehigh University, Bethlehem, Pennsylvania 18015, USA and Advanced Imaging & Microscopy Laboratory, Maryland NanoCenter, Institute for Research in Electronic and Applied Physics, University of Maryland, College Park, Maryland 20742, USA*
[2]*Department of Materials and Mineral Resources Engineering, National Taipei University of Technology, Taipei 10608, Taiwan*
[3]*Institute of Mineral Resources Engineering, National Taipei University of Technology, Taipei 10608, Taiwan*
[4]*Material Measurement Laboratory, National Institute of Standards and Technology, Gaithersburg, Maryland 20899, USA*
[5]*Reliability Assessment Center for Chemical Materials, Korea Research Institute of Chemical Technology, Daejeon 34114, Korea*
[6]*Institute of Materials Science and Engineering, National Taipei University of Technology, Taipei 10608, Taiwan*
[7]*Center for Condensed Matter Sciences and Center of Atomic Initiative for New Materials, National Taiwan University, Taipei 10617, Taiwan and Taiwan Consortium of Emergent Crystalline Materials, National Science and Technology, Taipei 10622, Taiwan*

(Received 7 March 2023; revised 25 April 2023; accepted 5 May 2023; published 7 June 2023)

Monoclinic hafnia (m-HfO_2) with its high dielectric permittivity (κ) and larger band gap of ~5.5-5.9 eV deposited as a few nanometers thick m-HfO_2 thin film on a Si substrate was introduced as an effective gate oxide in complementary metal-oxide-semiconductor devices by Intel in 2007. However, the existence and complex anisotropic excitation characters of this centrosymmetric monoclinic crystal structure—which involve both single-particle and collective electron excitations such as plasmons, and include electron-hole (excitonic) and electron-electron (self-energy) interactions—remain elusive. Therefore, the electronic nature of the material needs to be explored in depth for applications in semiconductor technology. In this study, spatially and momentum-resolved electron energy-loss spectroscopy (EELS) in conjunction with first-principles calculations of the electronic band structure and dielectric function have been employed to investigate electronic excitations in m-HfO_2. The phase purity and crystallinity of m-HfO_2 were confirmed by x-ray diffraction and EELS. Low-loss EELS performed using *aloof* electron beam setups and energy-filtered transmission electron microscopy spectrum imaging (EFTEM-SI) revealed spectral features at 13.5 and 16 eV energy loss assigned to surface plasmons and volume plasmons (VPs), respectively. Surface exciton polaritons (SEPs) with surface resonances associated with excitonic onsets above the band gap were also observed at ~7.5 and ~28 eV energy loss. The surface excitation character of these features was confirmed by EFTEM-SI and relativistic calculations of energy versus momentum (E-k) maps. Using collection-angle (β) and momentum (q)-resolved EELS, it was found that the SEP intensity at ~7.5 eV energy loss is a function of β and q, and no anisotropic shape for the VP is observed along the [100], [010], and [001] directions. Furthermore, the peak at ~48 eV energy loss was assigned to a semicore Hf 5p plasmon involving multiplet resonant processes. All the VPs, the SEPs at 28 eV energy loss, and the Hf 5p plasmons at 48 eV energy loss display parabolic dispersion behavior with an energy shift of 1–3 eV.

DOI: 10.1103/PhysRevMaterials.7.065201

I. INTRODUCTION

To follow Moore's law, the dimensions of complementary metal-oxide-semiconductor (CMOS) devices and metal-oxide-semiconductor field-effect transistors (MOSFETs) in ultralarge-scale integrated (ULSI) circuits should continue to scale down. At this moment, the conventional gate oxide (SiO_2 with $\kappa \sim 3.9$) meets the physical limitations. To improve the drain-current response of the transistors to the applied gate voltage, the thickness of SiO_2 should be less than 1.3 nm. A significant leakage current would arise when the thickness of SiO_2 is less than 1 nm because of a not well-developed electronic structure unlike in the bulk material [1]. Let us consider the capacitance formula $C = \kappa\varepsilon_o(\frac{A}{D})$ where κ is the dielectric constant, ε_0 is the dielectric constant for vacuum, A is the gate area, and D is the gate thickness. Because the gate area A becomes smaller with downscaling, the high-κ dielectric material should be considered to keep the similar capacitance C. Thus, hafnia (HfO_2) with its large band gap (5.5-5.9 eV) [2,3] and high κ values equal to ~29 for cubic, ~70 for tetragonal, and ~16 for monoclinic phase, respectively [4], was successfully used to replace the SiO_2, starting from the 45 nm node process released by Intel in 2007 [5]. The value of $k = 16$ for monoclinic HfO_2 (m-HfO_2)

---

[*] szl223@lehigh.edu
[†] gjshu@mail.ntut.edu.tw

suggests a ∼4 nm thickness to satisfy the requirement for a 1 nm equivalent oxide thickness (EOT) sufficient to prevent current leakage. Here, the EOT $= t_{\text{high}-\kappa}(\frac{\kappa_{SiO_2}}{\kappa_{\text{high}-\kappa}})$ where $t_{\text{high}-\kappa}$ is the thickness of high-κ dielectrics and $\kappa_{SiO_2} = 3.9$ is the dielectric constant for SiO_2.

It is well known that HfO_2 undergoes several polymorphic structural transformations with temperatures from high-symmetry cubic phase (space group $Fm\bar{3}m$), stable above 2370 °C, to slightly distorted tetragonal phase (space group $P4_2/nmc$), found at 1170 °C–2370 °C, and to monoclinic phase (space group $P12_1/c1$) existing from room temperature to ∼1170 °C [4,6]. Pressure-driven transformation of HfO_2, from the monoclinic phase to the high-pressure orthorhombic I phase (space group *Pbca*) at 4 GPa and orthorhombic II phase (space group *Pmnb*) at 14.5 GPa, has also been reported [7]. All of the HfO_2 phases, including cubic, tetragonal, orthorhombic, and monoclinic, are the centrosymmetric nonpolar phases and, thus, do not include spontaneous polarization needed for ferroelectric response. Recently, an unexpected orthorhombic III (orthoIII) phase representing a noncentrosymmetric polar structure with the space group of $Pca2_1$ was obtained using doped HfO_2 films confined with capping layers during thin film growth [8–10], hinting at a need for further investigation of the potential of HfO_2 as ferroelectric material. The tetragonal, orthorhombic, and monoclinic structures can be considered as distorted cubic ones and described as a fluorite structure, and, similar to polymorphic ZrO_2 [11] and TiO_2 [12], reflected just a few tiny differences in their electronic structures compared to cubic HfO_2. Therefore, in this work, we mainly focus on the study of the electronic structure of the m-HfO_2 that can be obtained relatively easily at ambient temperature and pressure compared to the other phases.

Only a few reports have been published on the electronic excitations of m-HfO_2 investigated by electron energy-loss spectroscopy (EELS). The low-loss EEL spectrum usually displays several predominant spectral features at 15–16 eV, 26–29 eV, 35–37 eV, and about 48 eV energy loss [3,13–18]. The spectral feature at about 15–16 eV energy loss had been interpreted as a volume plasmon (VP) [13–15,17,18], and the features between 35 and 37 eV energy loss were assigned to the well-known minor Hf $O_{2,3}$ edge [13–15,17,18]. However, some controversy remains concerning the interpretation of the physical origin of the rest spectral features. Features at about 26–29 eV energy loss have been explicated as collective excitations [14,18] or interband transitions [16] while the features at about 48 eV energy loss have been assigned to the Hf $\boldsymbol{O}_{2,3}$ edge [14] or local field-effect-damped plasmon [18].

Recently, the anisotropy of electron excitations along different crystal orientations in m-HfO_2 was analyzed using the energy-filtered transmission electron microscopy (EFTEM)–valence EELS technique (also known as EFTEM-SI) with a specimen thickness of 15–40 nm [18,19]. The VP at 16 eV energy loss revealed the anisotropy which appears as a predominant peak along the [001] direction whereas a broadened feature was observed along the [100] and [010] directions. In addition, the oscillator strength of the VP at 16 eV energy loss was weaker than that of the spectral feature at ∼28 eV energy loss assigned to the collective excitation [15,18,19]. Furthermore, the opposite observations indicating the oscillator strength of the VP are higher than that for the 28 eV peak reported using scanning transmission electron microscopy (STEM) EELS with similar EELS acquisition conditions including collection β angles and similar specimen thickness [13–15]. Thus, some controversial interpretations and inconsistent observations of electronic excitations in m-HfO_2 remain, especially concerning anisotropic excitations in this centrosymmetric crystal structure.

In this study, to analyze electronic excitations in m-HfO_2, the phase purity and stoichiometry of m-HfO_2 were verified using x-ray diffraction (XRD) to avoid the deviations induced by different phases or oxygen vacancies. Then, electronic excitations in m-HfO_2 were systematically studied by low-loss EELS or so-called valence EELS with nonpenetrating incident electron beam (*aloof* excitation) in scanning transmission electron microscopy (STEM) mode and electron diffraction mode to analyze the electronic excitations as a function of EELS collection β angle and momentum (q) transfer. A*b initio* density functional theory (DFT) calculations were also performed to calculate the complex dielectric function $\varepsilon(\omega) = \varepsilon_1(\omega) + i\varepsilon_2(\omega)$ and corresponding EEL spectra along selected q-transfer directions.

II. EXPERIMENTAL APPROACH

m-HfO_2 powders (99.99% purity), ordered from Aldrich,[1] were used as a starting material, pressed as a pellet, and then sintered in air at a temperature above 1600 °C to form a compact m-HfO_2 disk. A Bruker D2 Phaser diffractometer with Cu source and LYNXEYE detector were used to determine the phase identification and structure analysis for the m-HfO_2 sintered disk. The data were collected at room temperature with 0.02° per step and a scanning speed of 0.5 s per step. The collected XRD patterns were analyzed with the Rietveld method using the Bruker DIFFRAC.TOPAS program package. TEM specimens were prepared using a tripod polishing technique and then thinned using Ar^+ ion milling operated at 5 kV until a hole formed, and then operated at 0.3 kV to remove the surface amorphous layers [20]. Microstructures and electronic excitations were examined in a JEOL-2100F (scanning) transmission electron microscope [(S)TEM] equipped with a Gatan Image Filter (GIF, Tridiem 863 model), operating at 200 kV. The energy resolution was 0.7 eV throughout the (S)TEM-EELS experiments. The momentum (q)-resolved EELS experiments were carried out in selected-area diffraction mode with q resolution of 0.015 Å^{-1}. Real-space energy-filtered TEM (EFTEM) spectrum imaging (SI) (EFTEM-SI) with a tunable energy-selection slit was conducted using the same microscope. The single-scattering EELS distributions were derived via deconvolution from raw EELS data, which was performed by removing the zero-loss peak either by fitting a premeasured zero-loss peak from the vacuum or by removing plural scattering with the

---

[1] Certain equipment, instruments, or materials are identified in this paper in order to adequately specify the experimental details. Such identification does not imply recommendation by the National Institute of Standards and Technology nor does it imply the materials are necessarily the best available for the purpose.

TABLE I. The refinement results of room temperature XRD pattern of HfO_2.

Space group = $P2_1/c$ (No. 14)
$a = 5.1198(1)$ Å, $b = 5.1750(2)$ Å, $c = 5.2957(2)$ Å,
$\beta = 99.192(2)^\circ$, and $V = 138.506(7)$ Å^3
$R_{wp} = 5.73\%$, $R_p = 4.58\%$, and GOF = 1.25

Atom	Site	x	y	z	Bq/Å^2
Hf1	4e	0.2755(2)	0.0395(1)	0.2083(2)	0.18(4)
O1	4e	0.080(2)	0.336(2)	0.344(2)	0.21(17)
O2	4e	0.445(2)	0.761(2)	0.478(2)	0.21(17)

Fourier-log method [21]. The subsequent Kramers-Krönig analysis (KKA) was conducted using the DIGITALMICROGRAPH software package (Gatan Microscopy Suite, Gatan-AMETEK) as described elsewhere [21–23]. The scattering probabilities of *aloof* STEM-EEL spectra as a function of an impact parameter were calculated using the equations and MATLAB scripts described in Refs. [24,25]. The dielectric data for m-HfO_2 were taken from the KKA results. Optical properties such as reflectance, absorbance, and band gap energy of HfO_2 were analyzed using an ultraviolet-visible (UV-Vis) spectrometer (JASCO V670 model, Japan) in the wavelength range from 200 to 1600 nm at room temperature.

Single-point energy calculations of m-HfO_2 were performed by using a Vienna *ab initio* simulation package (VASP) based on the density functional theory (DFT) [26–28]. The generalized gradient approximation (GGA) was used with the Perdew-Burke-Ernzerhof (PBE) [29,30] exchange-correlation functional and the projector augmented-wave (PAW) pseudopotentials [31,32]. Calculations of the electronic band structure and dielectric function with no band gap correction were employed to characterize the absorption of m-HfO_2. Lattice parameters and atomic positions in m-HfO_2 according to measured values are shown in Table I. The cutoff energy for the plane-wave basis set was set to 500 eV and a 12 × 12 × 12 Γ-centered k-point mesh was used in the calculations. The convergent criteria of the self-consistent field cycle for the electronic wave functions were set to be 10^{-8} eV for energy. To aid in interpreting the spectra, we present results that leave out and include local field effects (LFEs).

III. RESULTS AND DISCUSSION

To examine the crystal quality and structure of the HfO_2 pellet, x-ray powder diffraction (XRD) analyses were performed on HfO_2 powders that were extracted via crushing and grinding of a sintered HfO_2 pellet. The XRD pattern and the Rietveld refinement results are shown in Fig. 1(a). The representative TEM bright-field (BF) image, inset image in Fig. 1(b), shows that the grain size of the HfO_2 pellet ranges from a few hundred nanometers to a few micrometers scales. The detailed crystal structure parameters and atomic coordinates are listed in Table I. The XRD pattern and refinement results reveal that the HfO_2 sample used in this study is composed of a single monoclinic phase without any secondary phases such as orthorhombic, tetragonal, or cubic. The HfO_2 adapts a monoclinic structure with the space group of $P2_1/c$ (No. 14), where the hafnium and oxygen atoms all occupy the 4e (x, y, z) coordination sites. The satisfactory refinement results were obtained with fit factors of $R_{wp} = 5.73\%$, $R_p = 4.58\%$, and goodness of fit (GOF) = 1.25, which gave the lattice parameters $a = 5.1198(1)$ Å, $b = 5.1750(2)$ Å, $c = 5.2957(2)$ Å, and $\beta = 99.192(2)^\circ$, which are in good agreement with the values reported in the literature [33,34]. Since no apparent off stoichiometry was observed, the occupancies were set to be unity in the subsequent analyses. The HfO_2 structure [see inset in Fig. 1(a)] displays the distortion of the fluorite structure consisting of a HfO_7 polyhedron with all Hf-O bond lengths that range from 2.014(8) to 2.270(9) Å in good agreement with the reported values [33,34]. The Hf-O bond distances are summarized in Table II.

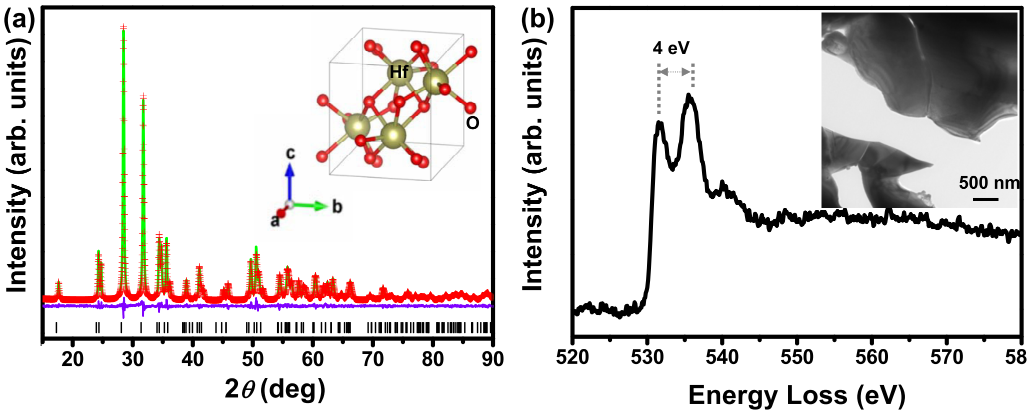

FIG. 1. (a) XRD pattern of m-HfO_2 recorded at room temperature and Rietveld refinement results. The inset shows the unit cell of m-HfO_2. (b) The ELNES of the O K edge of m-HfO_2. The Hf-O bonding distances calculated by Rietveld refinement from XRD pattern(a) are listed in Table II.

TABLE II. Hf-O bond distances in HfO_2 derived from refinement results.

	Bond length (Å)
Hf-O	2.014(8)
	2.085(8)
	2.138(8)
	2.145(8)
	2.158(8)
	2.220(8)
	2.270(8)

By examining the electron energy-loss near-edge structure (ELNES) of the oxygen (O) K edge, one can obtain direct information on the chemical coordination, O vacancies, and hence, the crystalline phase [21]. While the O K edge corresponds to the transitions from the O $1s$ core orbitals to the unoccupied O $2p$ states by following the dipole selection rule ($\Delta\ell = \pm1$, ℓ is an angular quantum number) [21], the O K-edge spectrum of HfO_2 is influenced by the hybridization of the Hf $5d$ states and the O $2p$ states. The O K-edge ELNES of m-HfO_2 in Fig. 1(b) displays distinct and well-defined double peaks separated by 4.0 eV, which are consistent with reports [35,36]. While inspecting the ELNES, a few points of interest should be noted. First, the doublet peak shape of the O K edge in m-HfO_2 is usually assigned to the crystalline HfO_2 [35]. Second, the doublet peaks with peak separation in m-HfO_2 result from crystal-field splitting [35,36]. Indeed, the m-HfO_2 can be described as a distorted fluorite structure, where the Hf atoms are surrounded by seven equivalent O atoms to form the distorted HfO_7 polyhedra [see inset in Fig. 1(a)] with all Hf-O bond lengths unequal [see Table II]. Despite the relatively low crystal symmetry ($P2_1/c$) contrary to the cubic HfO_2 with space group of $Fm\bar{3}m$, the ligand field splitting of the Hf $5d$ orbitals, which are hybridized with the O $2p$ orbitals, retains a broadened well-defined splitting into two manifolds, i.e., e_g and t_{2g}, that occurs in the cubic (HfO_8) fluorite environment. Finally, the spectral strength of the first peak is more than the half height of the secondary peak, and the peak height ratio was 0.87, which is higher than the values reported earlier for m-HfO_2 films (<0.81) [35–38]). It has been found that O-deficient HfO_2 samples usually show a broader and weaker first peak or even a shoulder in the O-K edge due to their defective structure [35,39]. Therefore, the higher intensity ratio between the two peaks indicates fewer O vacancies and, thus, this confirms the presence of stoichiometric m-HfO_2.

Next, valence EELS measurements were then performed in the STEM mode (STEM-EELS) with a 2 Å electron probe to not only preserve the spatial resolution but also to use nonpenetrating electron beams, i.e., an *aloof* setup [21,23]. This setup can allow one to sequentially position the probe at different positions along a chosen direction from the material interior to the vacuum. Figure 2(a) shows EEL spectra of the bulk m-HfO_2 for different values of the impact parameter b recorded at the different positions from the material interior ($b = -14$ nm and calculated thickness is ∼50 nm) to the vacuum ($b = 20$ nm) (negative b, from edge to material interior; positive b, from edge to the vacuum; $b = 0$ nm, edge), as indicated by the circles in the STEM high-angle annular dark field (HAADF, STEM HAADF) image in Fig. 2(c). When positioning the electron probe at $b = -14$ nm, i.e., in the material interior [orange circle in the STEM HAADF image in Fig. 2(c)], several broad spectral features above the optical band gap are observed at about 8, ∼16, ∼20.7, and ∼28.5 eV energy loss (marked as black arrows), which is in good agreement with the reports [15–18]. Features at the energy below 30 eV energy loss in HfO_2 are primarily associated with collective excitations of the valence and conduction bands, while those above 30 eV energy loss can be assigned to the core-loss Hf $\boldsymbol{O}_{2,3}$ edges.

It is well known that low-loss EEL spectra of materials can be understood in the framework of the macroscopic complex dielectric function $\varepsilon(\omega) = \varepsilon_1(\omega) + i\varepsilon_2(\omega)$. The $\varepsilon(\omega)$ of m-HfO_2 was derived from the bulk spectrum [orange spectrum in Fig. 2(a)] by performing the KKA. Its real and imaginary parts shown in Fig. 2(b) indicate consistency with the literature reports [15,16]. The ε_1 curve in Fig. 2(b) rises to the maximum at about 5.3 eV energy loss and then vanishes with the negative slope. Furthermore, it vanishes again with a positive slope at 12.8 eV energy loss and then crosses the energy-loss axis at 15.7 eV energy loss. Therefore, the spectral feature at about 16 eV energy loss in Fig. 2(a) can be interpreted as a VP since it satisfies the criterion of $\varepsilon_1 = 0$ with the positive slope and small ε_2 value [15–17,21,23,40]. In contrast to the feature at 16 eV energy loss, ε_1 is nonzero at about 28.5 eV energy loss, which is consistent with other experiments [15,16] and the theoretical calculations [16,19]. This means that the peak at about 28.5 eV energy loss cannot be interpreted as a VP although some reports assigned this spectral feature to collective excitations [14,15,18,19]. Upon further inspection, ε_2 in Fig. 2(b) reveals an absorption maximum peak at about 6.2 eV energy loss and a weaker feature at about 11 eV energy loss that arises in this energy range from excitonic or/and interband transition excitations. Additionally, a series of high-energy interband transitions associated with the O $2s$ or the Hf $4f$ electron states [41,42] induce several broad maxima in ε_2 between 17 and 25 eV energy loss [see enlarged scale inset in Fig. 2(b)].

To investigate surface-induced resonances such as surface plasmons (SPs) and related excitations of excitons, valence EELS measurements were carried out using the *aloof* electron beams, while sequentially shifting the probe position in the direction from the material interior to the specimen edge at grazing incidence (i.e., from $b = -14$ nm to $b = 0$ nm) within a few nanometers away from the specimen edge. Spectra in Fig. 2(a) indicate that not only do both features at around 16 eV and around 28.5 eV energy loss decrease their oscillator strengths but the peak at 16 eV shifts to about 13.5 eV at $b = 0$ nm [see the dark yellow spectrum in Fig. 2(a)], while the peak at 28.5 eV only vanishes and then transforms into a broader feature. When the electron probe was positioned at the specimen edge at grazing incidence [i.e., $b = 0$ nm; see the dark yellow spectrum in Fig. 2(a)], the oscillator strength of the VP significantly decreased, while the peak at 13.5 eV energy loss (marked with a blue arrow) was enhanced. Then, the oscillator strength of the peak at 13.5 eV energy loss decreased with increasing the b values

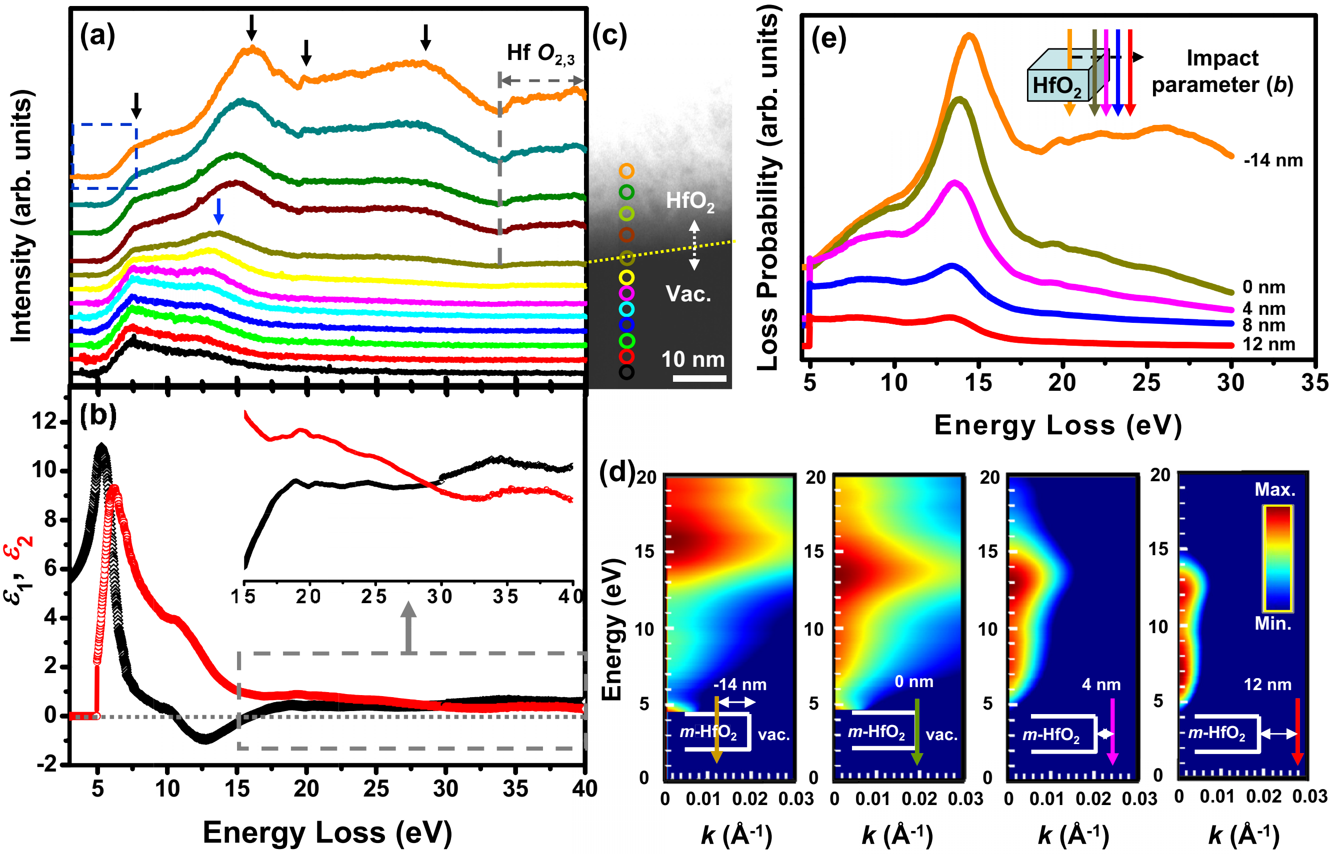

FIG. 2. (a) *Aloof* beam low-loss STEM-EEL spectra acquired from *m*-HfO_2 with the electron probe positioned at the locations marked in the STEM image in (c). The color circles denote probe positions in the inset. Corresponding EEL spectra are shown in the same colors. (b) The real (black) and imaginary (red) parts of the dielectric permittivity of *m*-HfO_2 derived from the orange spectrum in (a). (c) shows the STEM-HAADF image with locations marked for aloof low-loss STEM-EEL spectra. (d) The calculated relativistic E-k intensity maps for 50 nm thick *m*-HfO_2 slab with impact parameters $b = -14$, 0, 4, and 12 nm. The electron probe position exploited for the calculations is depicted in each corresponding inset. (e) The calculated relativistic loss probabilities of 50 nm thick *m*-HfO_2 slab per unit electron path length integrated over k in the 0-0.03 Å^{-1} range with impact parameters $b = -14$, 0, 4, 8, and 12 nm.

from 0 to 6 nm, away from the surface [see yellow, pink, and cyan spectra in Fig. 2(a)] indicating its surface excitation character. Here, electromagnetic waves propagate at the material surface with the evanescent wave fields exponentially decaying into the bound media (or vacuum) and material [11,15,16,21,23,40]. The nature of such excitations is manifested by negative values of ε_1 observed in this energy range [see Fig. 2(b)]. The peak at 13.5 eV energy loss can be therefore interpreted as a SP [11,15,16,21,23,40]. The broad shoulder at about 8 eV energy loss decreased slower than the SP at 13.5 eV energy loss with a sequential shifting of the electron probe from the specimen edge into the vacuum [see spectra in Fig. 2(a)]. The shoulder at about 8 eV energy loss further remains a prominent spectral onset, confirming the surface character of the related excitations. Indeed, this feature was interpreted as an interband transition from the O 2p to the Hf 5d states [13,19,41]. Moreover, since the criterion of $\varepsilon_2 > \varepsilon_1 > 0$ [17,23] is satisfied, this feature, occurring near interband transitions, bears a strong resemblance to the excitations of surface exciton polaritons (SEPs), which are collective oscillators of delocalized excitons at the surfaces of materials.

For comparison with experimental EEL spectra in Fig. 2(a), relativistic E-k maps were calculated [24,25] as a function of impact parameter b for a 50 nm thick *m*-HfO_2 layer [see Fig. 2(d)]. Figure 2(e) also shows calculated relativistic loss probabilities per unit electron path length along the electron trajectory and integrated over the k range up to 0.03 Å^{-1}. The calculated E-k maps and spectra in Figs. 2(d) and 2(e) reveal the predominant VP at about 15 eV energy loss when the electron probe was positioned inside the slab at $b = -14$ nm. When the electron probe was sequentially located at the edge at grazing incidence ($b = 0$ nm), the SP at about 13.5 eV energy loss was strongly enhanced, and the probe position was away from the edge ($b = 4$, 8, 12 nm); the features decrease its oscillator strength, indicating its surface character in the presence of evanescent wave fields. The calculations also successfully reproduced the SEP at about 8 eV energy loss at $b \geqslant 4$ nm. Both calculated E-k maps and corresponding EEL spectra appear in good agreement with the experimental results (see Supplemental Material [43]).

Figure 3(a) shows an enlarged part of the orange EEL spectrum in Fig. 2(a) redrawn to illustrate the band gap measurements. The optical band gap (E_g) of about 5.7 eV was

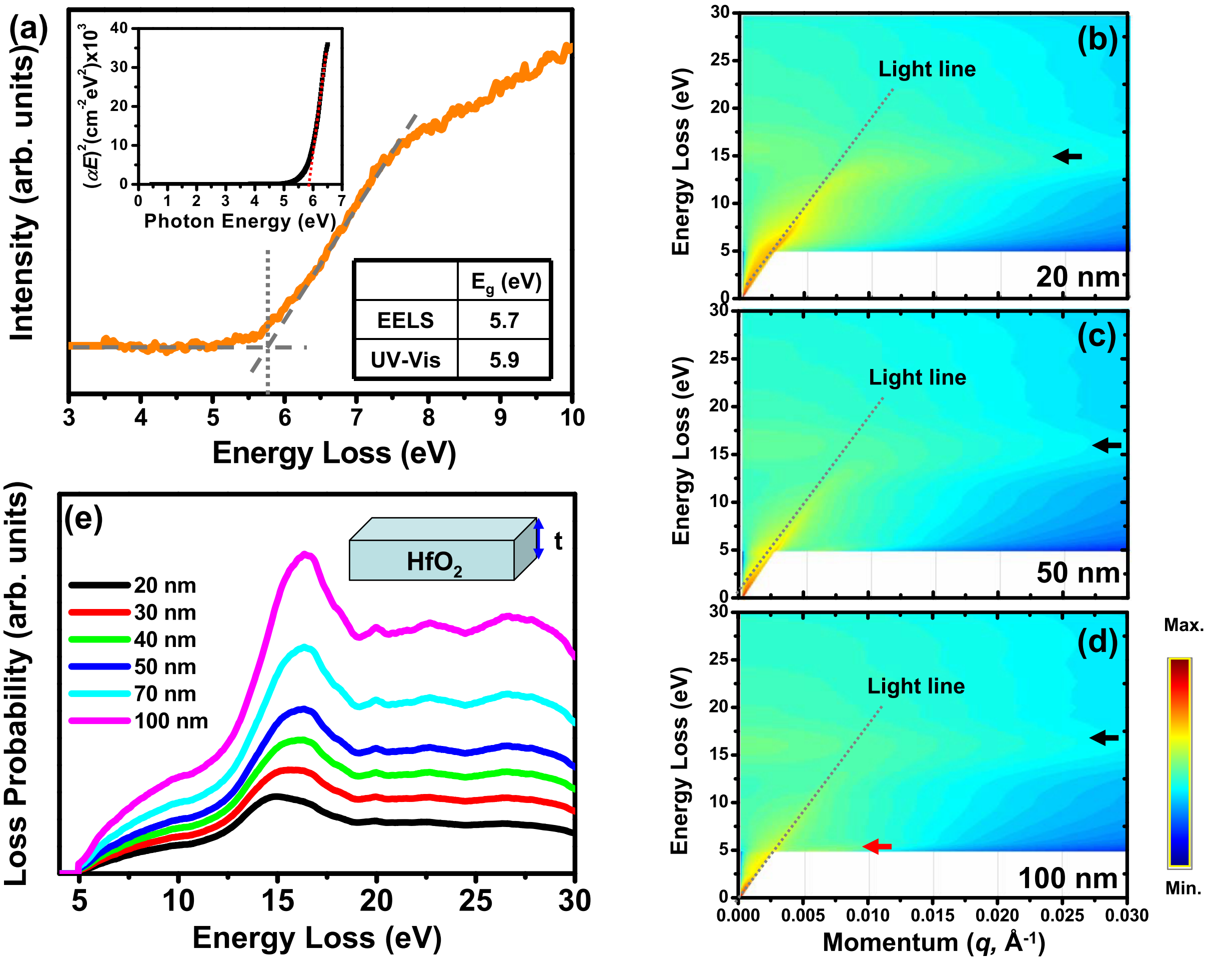

FIG. 3. (a) The EEL spectrum in Fig. 2(a) redrawn to illustrate the band gap measurements. Inset is Tauc's plot for the band gap analysis of *m*-HfO$_2$ from the optical absorption data measured at room temperature. The calculated relativistic E-k maps (E is energy loss and k is momentum transfer) for *m*-HfO$_2$ slabs with thicknesses of 20 nm (b), 50 nm (c), and 100 nm (d) at accelerating voltage of 200 kV. (e) The calculated relativistic loss probabilities of *m*-HfO$_2$ slab per unit electron path length integrated over k in the range of 0–00.3 Å^{-1} for the thickness of 20, 30, 40, 50, 70, and 100 nm.

determined using the linear fitting method [23,44], and no additional features were found in the band gap that might be due to the oxygen vacancies or interstitial-related defects with divalent or trivalent cation dopants [45]. It is well known that the E_g may shift to the lower energies with increasing the specimen thickness due to the excitation of Cherenkov radiation (CR) because the CR can be excited if $\varepsilon_1(v/c)^2 > 1$ [21–23,40,46]. Here, v is the velocity of incident electrons and c is the velocity of light. Since in our experiments were performed at 200 kV accelerating voltage with $v \sim 0.7c$ and at a larger ε_1 value of ∼11 [see Fig. 2(b)], this condition can be satisfied.

To evaluate the CR effect, we first calculated the relativistic energy versus momentum (E-k maps) for *m*-HfO$_2$ slabs of 20, 50, and 100 nm in thickness. The calculations have been performed using Kröger's equation [47] at the accelerating voltage of 200 kV close to experimental conditions, shown in Figs. 3(b)–3(d). The related relativistic loss probabilities per unit electron path length along the electron trajectory and integrated over the k range up to 0.03 Å^{-1} are shown in Fig. 3(e). From the calculated E-k maps and the related relativistic loss probabilities, we found that the plasmon peak shifts its energy from 14.5 eV energy loss to ∼16 eV energy loss (marked by the black arrows) and also enhances its intensity with the thickness increased from 20 to 100 nm. For the 50 nm thick *m*-HfO$_2$ slab, the CR excitation does not induce distinct dispersion features near the band gap onset below 5 eV, unlike the significant dispersion feature that appears for 100 nm thick *m*-HfO$_2$ slabs. Thus, EEL spectra were therefore acquired in areas of the material interior with a sufficient thickness of 50 nm to minimize the CR excitation in the spectral region below 6 eV energy loss and simultaneously suppress the surface excitations [23,48]. For the same purpose, ultraviolet-visible (UV-Vis) spectroscopy was employed to determine the optical properties of the *m*-HfO$_2$ powders, including E_g, and compare them with EEL data.

UV-Vis spectroscopy is widely used to measure the absorption or reflectance spectra of materials at the wavelengths in the UV-visible light regions. The optical absorption in the shorter wavelength region is mainly attributed to the electron

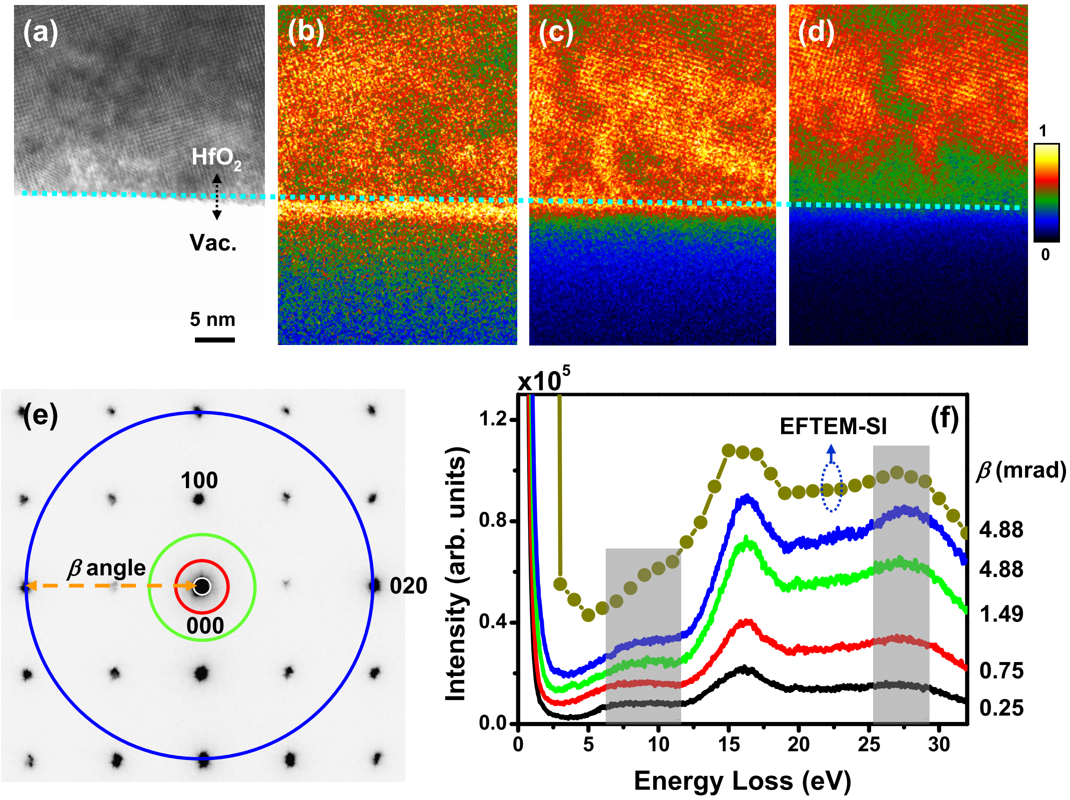

FIG. 4. (a) Zero-loss EFTEM image. (b)–(d) The EFTEM-SI intensity maps acquired at energy losses of 8 ± 1 eV (b), 13 ± 1 eV (c), and 16 ± 1 eV (d). The color scale bar represents the linearly normalized image intensity. (e) SAED pattern of m-HfO$_2$ recorded at the zone axis of [001] complementary to the HRTEM image in (a). The color circles indicate the different collection β angles used for recording the EEL spectra, and corresponding EEL spectra are shown by the same colors in (f). The extracted energy-loss spectrum from the EFTEM-SI datasets was plotted with a yellow-green dotted line for comparison. The intensities of the spectra were normalized to zero-loss peak and then vertical shifted to easily visualize.

transitions from the top of the valence band to the bottom of the conduction band. The absorbance and photon energy are related via the following equation [49],

$$(\alpha E)^n = A(E - E_g), \tag{1}$$

where α is the absorption coefficient, A is a constant, E_g is the optical band gap, and n is a constant associated with the different electronic transitions, where $n = \frac{1}{2}$ for indirect allowed transitions and $n = 2$ for direct allowed transitions, respectively. The E_g can be obtained from the extrapolation of the straight-line portion of $(\alpha E)^n$ versus E plot to $E = 0$, as shown in Fig. 2(d). As m-HfO$_2$ has been reported as a direct band gap material [50], the E_g of m-HfO$_2$ was calculated by using $n = 2$ and extrapolating the linear portion of the curve or tail [see inset in Fig. 3(a)]. The obtained value of $E_g = 5.9 \pm 0.02$ eV for m-HfO$_2$ is in good agreement with the results reported in the literature [50,51]. The electronic band structure of m-HfO$_2$ was calculated using *ab initio* DFT theory giving values of the indirect band gap of 4.0 eV and for the direct band gap of 4.3 eV, respectively. An underestimation of the calculated band gap energy in comparison to the experimental value can be explained by the well-known systematic error in the used DFT calculation scheme.

The SEP, SP, and VP excitations in m-HfO$_2$ have been also investigated using real-space spectrum imaging in the EFTEM mode (EFTEM-SI). In these experiments, a 2 eV energy-selection slit was positioned at 8, 13, and 16 eV energy loss [see in Figs. 4(b)–4(d)], where the corresponding spectral features at 8, 13.5, and 16 eV energy loss are located. The high-resolution transmission electron microscope (HRTEM) image of the same area oriented along the [001] direction towards the incident beam is shown for comparison in Fig. 4(a). The intensity maxima represent the spatial distribution of the SEP at 8 eV energy loss [Fig. 4(b)] and of the SP at 13.5 eV energy loss [Fig. 4(c)] that reveal the expected localization of SEPs and SPs at the edge of m-HfO$_2$ where the evanescent wave field was decaying into the vacuum exhibiting SP-like excitations. In contrast, the EFTEM-SI distributions of the VP at 16 eV [Fig. 4(d)] and 28.5 eV energy loss (not shown here) appeared strongly localized within the bulk interior, ambiguously indicating the volume resonance excitations. Furthermore, the onset of the peak at 28.5 eV energy loss closely correlates with the broad feature in ε_2 at 27 eV energy loss and the corresponding oscillating ε_1 structure [see Fig. 2(b)]. Since the aforementioned condition $\varepsilon_2 > \varepsilon_1 > 0$ was satisfied here, the spectral feature at about 28.5 eV energy loss can also be assigned to the excitation of SEPs in m-HfO$_2$.

Indeed, the EEL spectrum extracted from the EFTEM-SI dataset in Fig. 4(f) is similar to one recorded using STEM-EELS [see the orange spectrum in Fig. 2(a)]. The collection angle (β angle) used for the EFTEM-SI experiment is about 4.88 mrad. Figure 4(e) presents the selected-area electron

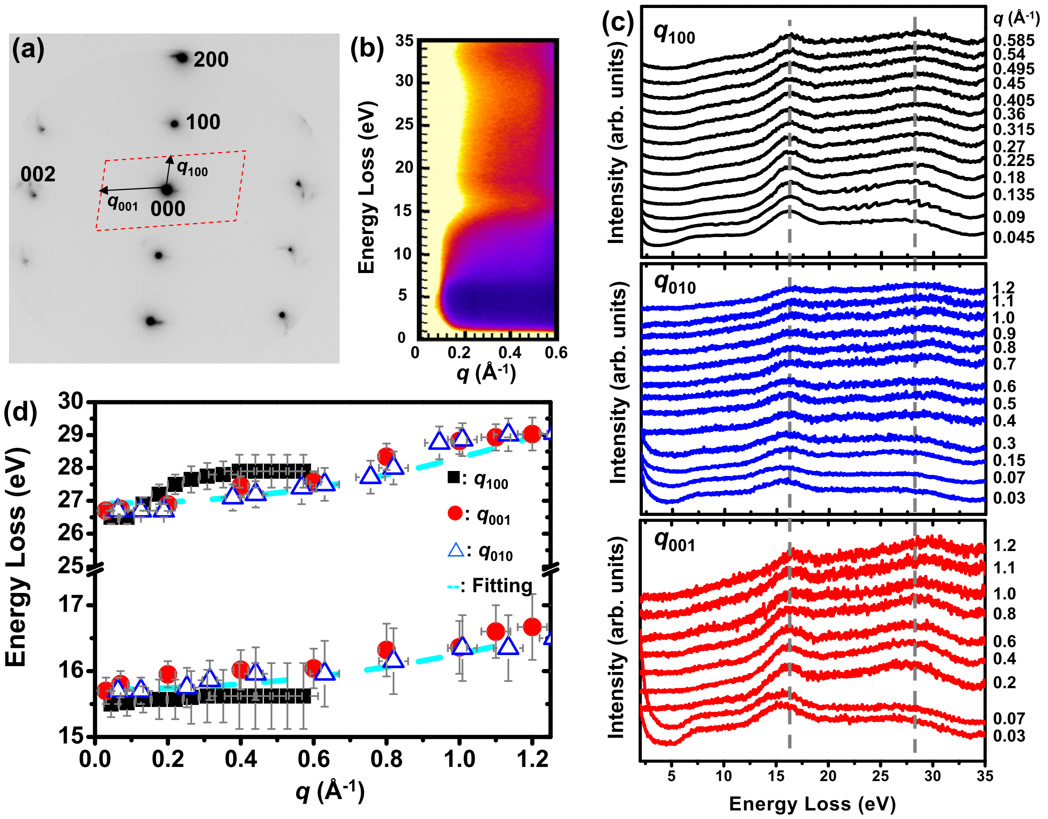

FIG. 5. (a) SAED pattern of m-HfO$_2$ recorded at the zone axis of [010]. (b) The ω-q map recorded along the [100] direction to the BZ boundary (~0.6 Å^{-1}). Momentum (q)-resolved EEL spectra collected with the q parallel to the [100] [top panel in (c)], [010] [middle panel in (c)], and [001] [bottom panel in (c)] directions. The spectra are all normalized by the intensity of the peak at ~15 eV and then displaced vertically to improve readability. (d) The energy of the VP at ~16 eV energy loss and the SEP at ~28.5 eV energy loss along the [100] (black square), [010] (red circle), and [001] (blue triangle) directions as a function of q.

diffraction (SAED) pattern taken along the [001] zone axis from the same area as the HRTEM image in Fig. 4(a). Figure 4(f) also shows the EEL spectra recorded for different collection β angles by adjusting the camera lengths in diffraction mode. From the inspection of the spectra in Fig. 4(f), a few interesting findings should be pointed out. First, the excitations of the SEPs (at about 8 and about 28.5 eV energy loss) and of the VP (at about 16 eV energy loss) increase their oscillator strengths with increasing the collection β angles. Therefore, the oscillator strength of the SEP at 28.5 eV energy loss increased rapidly to become near the same intensity as the VP at a β angle of 4.88 mrad. Second, the plateau between 5 and 10 eV energy loss was observed at $\beta < 0.75$ mrad, and then increased oscillator strengths enhanced the SEP features at about 8 eV energy loss at $\beta > 1.49$ mrad [see left shadowed region in Fig. 4(f)]. Intriguingly, the higher oscillator strength of the SEP at about 28.5 eV energy loss compared to that of the VP was observed in the orientation dependence and the polycrystalline case by performing the EFTEM-SI measurements with a smaller collection β angle of ~3 mrad [18,19]. Unlike for $\beta < 1$ mrad, the β angle of 4.88 mrad, as shown in Fig. 4(e), covers the (100) and (020) Bragg reflections in m-HfO$_2$, thus averaging out the EELS spectra for this crystal symmetry. To investigate possible electronic anisotropy along the different momentum (q) transfer directions, we performed momentum (q)-resolved EELS (q-EELS) experiments and studied the dispersion of spectral excitations under the diffraction mode using conventional TEM.

Momentum (q)-resolved EELS (q-EELS) is a powerful method to understand the anisotropy of the band structure and related electron excitations in a solid under varying momentum transfer ($\Delta\boldsymbol{q}$) and energy loss ΔE conditions [21,40]. Figure 5(a) presents the SAED pattern taken along the [010] direction of m-HfO$_2$ displaying the characteristic angle between the [001] and [100] directions of ~99.2° in the cell. Figure 5(b) shows the ω-q maps acquired in m-HfO$_2$ along the [100] direction to the Brillouin zone (BZ) boundary (~0.6 Å^{-1}). Figure 5(c) demonstrates q-EELS spectra obtained along the [100], [010], and [001] directions up to the BZ boundary of ~0.6, ~1.2, and ~1.2 Å^{-1}, respectively. From the spectra in Fig. 5(c), a few interesting findings should be pointed out. First, the VP at about 16 eV energy loss displays nondispersive behavior along the [100] direction and dispersive behavior along the [001] direction. Meanwhile, the SEP at about 28.5 eV energy loss also exhibits dispersive behavior in both directions. Second, the plateau feature between 5 and 10 eV energy loss is observed at $q < 0.14$ Å^{-1} and $q < 0.2$ Å^{-1} along the [100] and [010]/[001] directions, respectively. Then, its oscillator strength increases enhancing the SEP features at about 8 eV energy loss, which is similar to Fig. 4(f), at $q > 0.14$ Å^{-1} and $q > 0.2$ Å^{-1} along the [100] and [001] directions, respectively. It was also found that the band gap energy measured from the onset of the EEL spectra varies from ∼4.4 to ∼5.7 eV and from ∼5.1 to ∼5.7 eV along the [100] and [010]/[001] directions, respectively, implying the anisotropic band gap energy of the material. Finally, the oscillator strength of the SEP at about 28.5 eV energy loss increases with increasing the q values and becomes more intensive than the VP peak at $q > 0.8$ Å^{-1} along both the [001] and [010]/[001] directions. Most importantly, the VP peak at ∼16 eV energy loss looks well defined along the [100], [010], and [001] directions, thus indicating no significant anisotropy in peak oscillator strength.

To illustrate the underlying dispersion relations, Fig. 5(d) shows the dispersions of the VP at ∼16 eV energy loss and of the SEP at ∼28.5 eV energy loss with respect to the characteristic q, where the excitation energies were derived by Lorentz curve fitting [20,23]. One can first note that the VP displays almost nondispersive behavior along the [100] direction while the SEP reveals nonlinear q dependence at $q < 0.2$ Å^{-1}, and then turns to the nondispersive plateau until the BZ boundary of ∼0.6 Å^{-1}. In contrast, both the VP and the SEP along the [010] and [001] directions demonstrate less dispersion behavior at $q < 0.6$ Å^{-1} and then exhibit parabolic dispersion at $q > 0.6$ Å^{-1}. Indeed, after fitting the VP reveals the representative paraboliclike q^2 dependence along the [010] and [001] directions [see the bottom cyan dashed line in Fig. 5(d)]. Furthermore, for the [100] direction, the energies of the VP and the SEP increase from 15.5 to ∼15.6 eV energy loss and ∼26.5- ∼ 28 eV energy loss, respectively, while for the [010] and [001] directions, the energies shift from 15.7 to ∼16.7 eV energy loss and from ∼26.7 to ∼29 eV energy loss, respectively. Because the spectral features in the range from 17 to 25 eV energy loss represent interband transitions, the VP would transfer its energy to excite single-electron transitions and create the electron-hole pairs when the plasmon wave vector q exceeds the critical q_c value (i.e., 0.2 Å^{-1}, not shown here). The VP then starts damping followed by decreasing its oscillator strength and peak broadening. Consequently, the VP exhibits less energy shift of ∼1.2 eV with increasing q compared to the energy shift of the SEP, which is consistent with the theoretical calculations reported in Ref. [19]. Indeed, the SEP dispersion tends to follow a paraboliclike q^2 dependence, when q is larger than critical vector q_c [see the upper cyan dashed line in Fig. 5(d)].

For comparison with anisotropic features in experimental EEL spectra, dielectric properties of m-HfO$_2$ were calculated including the static dielectric tensor (ϵ_s) and high-frequency dielectric tensor (ϵ_∞) as follows:

$$\text{Static dielectric tensor } (\epsilon_s)$$
$$= \begin{bmatrix} 21.3578 & 0.0000 & 0.6316 \\ 0.0000 & 19.2565 & 0.0000 \\ 0.6316 & 0.0000 & 15.7394 \end{bmatrix},$$
$$\text{High-frequency dielectric tensor } (\epsilon_\infty)$$
$$= \begin{bmatrix} 4.9924 & 0.0000 & 0.07567 \\ 0.0000 & 4.9537 & 0.0000 \\ 0.07567 & 0.0000 & 4.6447 \end{bmatrix}.$$

Due to the primitive monoclinic symmetry of m-HfO$_2$ with the $P2_1/c$ space group [see Fig. 1(a) and Table I], the calculated dielectric tensors appeared to be neither diagonal nor have identical diagonal terms. Among the main directions, deviations were only 0.1759 Å (∼3.4%) for lattice lengths and 9.1918° (∼10.2%) for lattice angles, respectively. Hence, small anisotropies in m-HfO$_2$ can be found in any direction-dependent property since the calculated dielectric tensors had nonzero but small values of off-diagonal terms and similar values of diagonal terms. Some anisotropies in m-HfO$_2$ were found in the calculated frequency-dependent dielectric function $\varepsilon(\omega) = \varepsilon_1(\omega) + i\varepsilon_2(\omega)$ [see graphs in left panels, Figs. 6(b) and 6(c)] and the calculated EEL spectra [left panel in Fig. 6(a)] along the three main directions (i.e., $E//a$, $E//b$, and $E//c$) without LFE and with LFE. The experimental low-loss EEL spectrum of m-HfO$_2$ [inset in Fig. 6(a)] and the derived dielectric function $\varepsilon(\omega)$ (blue dashed curve) are also shown in Fig. 6 for comparison. First, one can see that the dielectric function near the absorption edge at ∼5 eV energy loss is similar in all directions with just small deviations in $E//a$, $E//b$, and $E//c$. Second, the absorption ε_2 curves for $E//a$ and $E//b$ reveal the broad feature at 5-10 eV energy loss, while a distinct peak exists at ∼9 eV energy loss for $E//c$ exhibiting the anisotropic absorption calculated without LFE. Indeed, the ε_2 curves for three main directions become rather close with considering the LFE in calculation. The ε_2 curves in the higher energy-loss range are similar. In contrast, the polarization ε_1 curves for $E//a$, $E//b$, and $E//c$ were close to the experimental results except for an additional shoulder that appears at ∼9 eV energy loss for $E//c$ calculated without LFE. Indeed, the ε_1 curves at ∼5.5 eV energy loss will change their feature from the distinct peak with a maxima value around 10 to a broadening feature with the value of 6 for all three main directions, without LFE and with LFE used in the calculation, respectively. Furthermore, the calculated EEL spectra for $E//a$, $E//b$, and $E//c$ orientations were similar to the experimental results except for the smaller energy of the edge onset (or E_g) in calculations. Indeed, the calculated EEL spectra demonstrate the similar shape and oscillator strength of the VP, which is consistent with experimental results in Figs. 4 and 5, although a small anisotropy in the dielectric function was found. Furthermore, the peak oscillator strength for SEP at ∼28 eV energy loss is close to the VP or slightly higher than the VP in contrast to the significant intensity difference in Refs. [18,19]. In general, both experimental results and theoretical calculations show a nearly isotropic dielectric response and the absorption in m-HfO$_2$ despite its anisotropy.

In addition, EEL spectra of m-HfO$_2$ display a puzzling spectral feature at ∼48 eV energy loss with full width at half maximum (FWHM), $\Delta E_{1/2}$ of ∼5.6 eV, and had been discussed as part of the Hf ***O*** edge [13,14] or a local field damped plasmon [19]. Intriguingly, similar spectral features above 40 eV energy loss were also observed in other fluorite-type structure materials, such as TiO$_2$ (at ∼46 eV energy loss with $\Delta E_{1/2}$ of ∼7 eV) [51] and ZrO$_2$ (at ∼41 eV energy loss with $\Delta E_{1/2}$ of ∼5 eV) [11,13]. These features were considered to be the excitations from the Ti 3p states to the Ti 3d states, and from the Zr 4p states to the Zr 4d states,

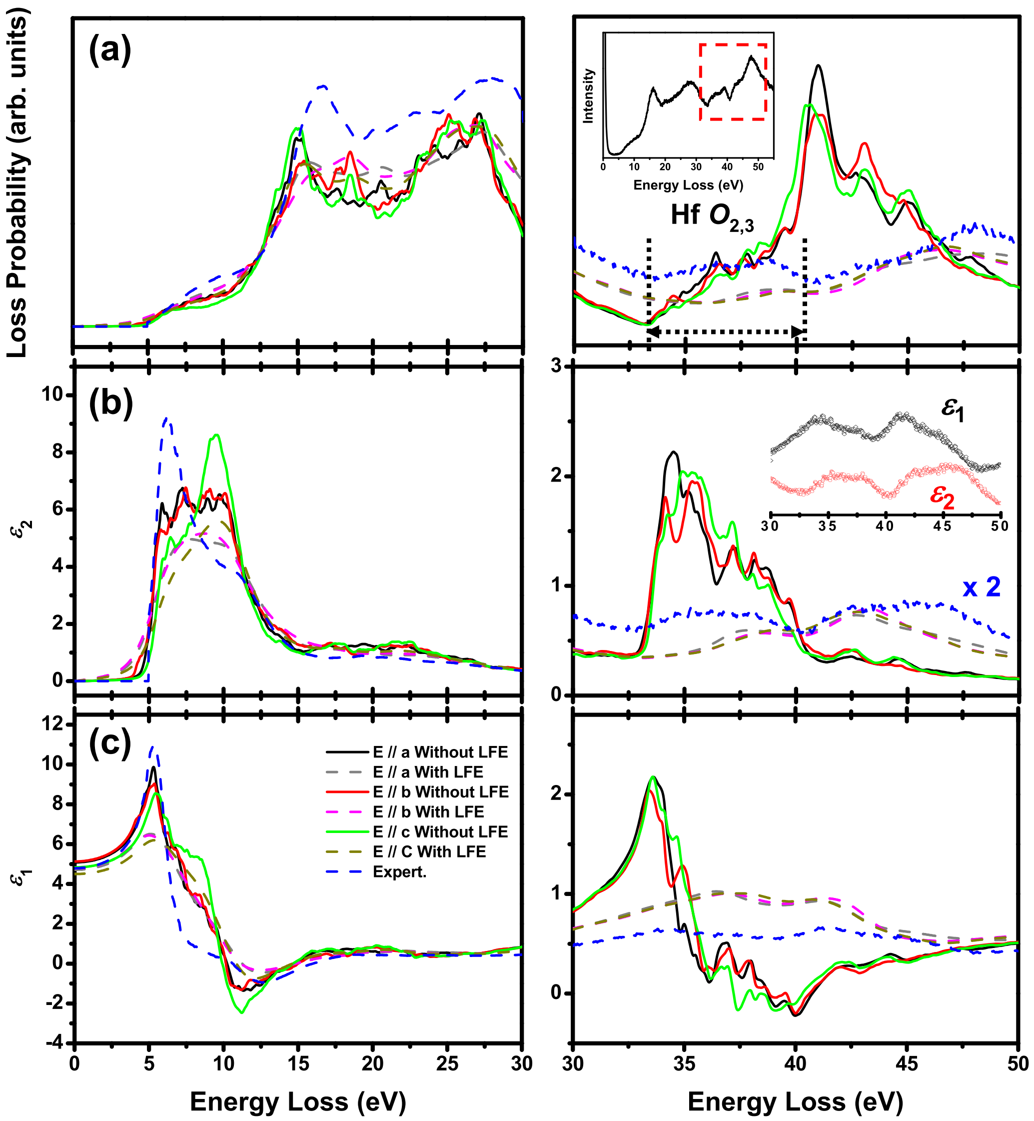

FIG. 6. (a) The energy-loss function, (b) the imaginary part of the dielectric function, and (c) the real part of the dielectric function for m-HfO$_2$ calculated along [100] (black curve and gray dashed line for calculated without and with LFE, respectively), [010] (red curve and pink dashed line for calculated without and with LFE, respectively), and [001] (green curve and dark yellow dashed line for calculated without and with LFE, respectively) directions. Experimental EEL spectrum [inset, the right panel in (a)], corresponding to the imaginary part and real part of the dielectric function, and calculated energy-loss function plotted with a blue dashed line for comparison. The inset, right panel in (b), is the enlarged real (black) and imaginary (red) parts of the dielectric permittivity of m-HfO$_2$ from Fig. 2(b).

respectively. Furthermore, the 3p (Ti) and 4p (Zr) to 5p (Hf) states are almost atomiclike but still are slightly hybridized with neighboring atoms causing minor chemical shift differences of less than 1 eV between metal and oxide states [11,52]. This was also confirmed by theoretical calculations considering the LFE [16,19,53,54].

Comparing the experimental and calculated $\varepsilon(\omega)$ at the high-energy-loss side [right panels in Figs. 6(b) and 6(c)], one can see distinct differences between the ε_1 and ε_2 curves. Here, the ε_1 derived from the experimental EEL spectrum is positive, while the calculated ε_1 without LFE crosses to the energy axis at ∼41 eV energy loss that corresponds to the spectral feature at ∼41 eV energy loss in the EEL spectrum in Fig. 6(a). However, the polarization ε_1 calculated with LFE reveals it is no longer negative in this region and does not cross zero which is similar to the earlier report in Refs. [16,19], where the feature was assigned to a local field damped plasmon based on the calculated $\varepsilon(\omega)$ and EEL spectrum using time-dependent density-functional theory (TDDFT) with LFE [19]. Therefore, the spectral feature at ∼48 eV energy loss cannot be directly interpreted as a VP [15]. Furthermore, the calculated ε_2 curves without LFE appear to be significant absorption features in the range of 32–40 eV energy loss, which is originally assigned as the Hf $O_{2,3}$ edge. However, the inclusion of LFE can lead to a dramatic improvement in the results, and reproduces the two absorption peaks at ∼37.5 and ∼43 eV energy losses, which is similar to the earlier report in Ref. [19] and close to the experimental ε_2 curves although there is the absence of the feature at ∼47 eV in all the calculations.

Indeed, the peak decays with the evanescent wave field into the vacuum at about 1 nm from the edge according to the

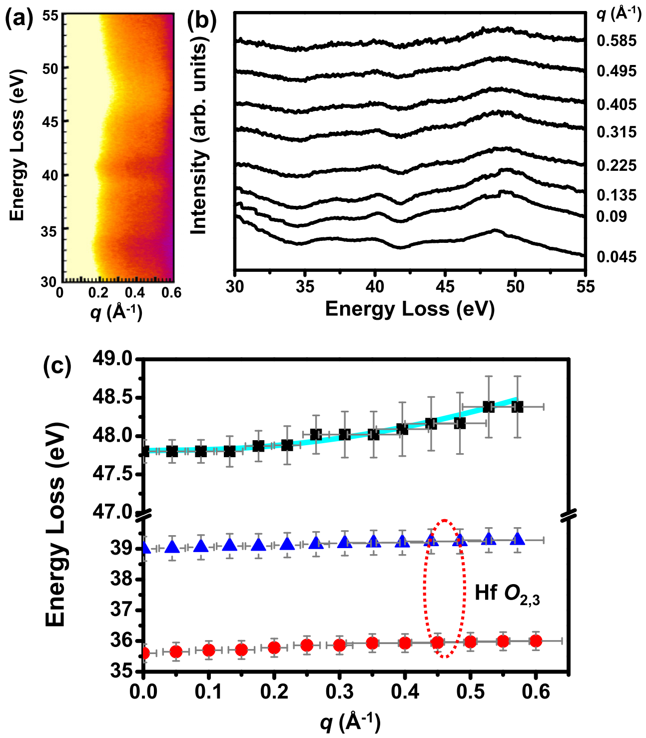

FIG. 7. The *ω*-*q* map for the energy-loss range 30-55 eV energy loss acquired along the [100] direction to the BZ boundary (∼0.6 Å^{-1}). (b) The EEL spectra extracted from the map (a) for different *q* values. (c) The energy of the Hf $O_{2,3}$ edge at ∼35 eV (red circle) and ∼39 eV (blue triangle), and the 5*p* semicore plasmon at ∼48 eV (black square) along the [100] direction as a function of *q*.

intensity profile in the corresponding EFTEM-SI image (not shown here). However, this decay length (l_d) of about 1 nm is shorter than the delocalization of 1.6 nm calculated using the formula $l_d = 0.5\lambda/(\theta_E^{3/4})$ [21], where λ is wavelength and θ_E is the relativistic characteristic angle, implying the peak at 48 eV energy loss can be only assigned to a bulk excitation.

Dispersion behavior of the major features in the higher energy-loss range (right panels in Fig. 6) is illustrated in Fig. 7. Figure 7(a) shows *ω*-*q* maps of the energy ranges from 30 to 55 eV along the [100] direction to the BZ boundary (∼0.6 Å^{-1}), and Figs. 7(b) and 7(c) show the EEL spectra extracted from Fig. 7(a) and dispersion of the peak at 48 eV energy loss as a function of characteristic *q*, respectively. The peak at 48 eV energy loss [Fig. 7(b)] reveals paraboliclike dispersion behavior along the [100] direction at $q > 0.1$ Å^{-1} with the energy shifts around ∼1 eV [see Figs. 7(a)–7(c)] while both the Hf $\boldsymbol{O}_{2,3}$ edges at ∼35 and ∼39 eV exhibit the nondispersive curves. The dispersions of the Hf $\boldsymbol{O}_{2,3}$ edges at ∼35 and ∼39 eV energy loss are also plotted for comparison. It is well known that either the VP or the SEP should demonstrate the paraboliclike dispersion while the nonvertical interband transition would display the linear dispersion curve [21,40,55]. Because the peak at 48 eV energy loss exhibits paraboliclike dispersion, the nonvertical interband transitions should be excluded. Upon further inspection, experimental ε_2 [right panel in Fig. 6(b)] exhibits an absorption peak at ∼47 eV energy loss that could be interpreted as an interband transition or the Hf 5*p* semicore excitation. However, at ∼47 eV energy loss $\varepsilon_2 < \varepsilon_1$ [see inset in the right panel in Fig. 6(b)] and therefore this feature cannot be assigned to the SEP.

Recently, the semicore 5*p* plasmons were proposed to interpret the peak at 48 eV energy loss for HfO_2 [19,53,54]. As aforementioned, these semicore electrons are slightly hybridized with neighboring atoms and therefore contribute to the partial valence bands (VBs). In this case, the resonance occurs as a multiplet process that involves electrons belonging to the partial VBs and single-electron excitations from the Hf $5p^6$ states to the $5p^5 5d^*$ states. Since the semicore Hf 5*p* plasmon is attributed to such multiplet resonance, it can easily damp via the single-electron excitation from the Hf $5p^6$ states to the $5p^5 5d^*$ states, still exhibiting the parabolic dispersion behavior with energy shift less than ∼1 eV. Because of the rapid damping rate with shorter relaxation time (*τ*), this results in broadening the peak since $\Delta E_{1/2} = \hbar/\tau$, where $\hbar$ is Planck's constant.

IV. CONCLUSIONS

The electronic excitations in monoclinic phase HfO_2 were systematically studied by spatially and momentum (*q*)-resolved EELS in STEM and SAED modes. By employing *aloof* electron beam setups and positioning the electron probe at the specimen edge in a grazing incidence and the material interior, respectively, the SP at ∼13.5 eV energy loss and the VP at ∼16 eV energy loss were observed. Using EFTEM-SI imaging and relativistic energy-momentum (*E*-*k*) map calculations, surface-related SEP excitations were revealed at ∼7.5 and ∼28 eV energy loss with an evanescent wave field decaying into the vacuum. *q*-resolved EELS shows that the SEP intensity at ∼7.5 eV energy loss is a function of collection *β* angle and *q*, and no anisotropy for the VP was observed along the [100], [010], and [001] directions. The peak at 48 eV energy loss was assigned to the semicore Hf 5*p* plasmons. The VP, the SEP at ∼28 eV energy loss, and the semicore 5*p* plasmon all display parabolic dispersion behavior with different energy shifts varying from 1 to 3 eV.

The data that support the findings of this study are available from the corresponding author upon reasonable request.

ACKNOWLEDGMENTS

G.-J.S. acknowledges the support of the National Science and Technology Council (NSTC), Taiwan under Project No. 111-2112-M-027-004-MY3, and part of this work was supported by the Taiwan Consortium of Emergent Crystalline Materials project with Funding No. 110-2124-M-002-019.

S.-C.L. and G.-J.S. contributed equally to the work.

---

[1] D. A. Muller, T. Sorsch, S. Moccio, F. H. Baumann, K. Evans-Lutterodt, and G. Timp, The electronic structure at the atomic scale of ultrathin gate oxides, Nature (London) **399**, 758 (1999).

[2] M. Balog, M. Schieber, M. Michman, and S. Patai, Chemical vapor deposition and characterization of HfO_2 films from organo-hafnium compounds, Thin Solid Films **41**, 247 (1977).

[3] M. C. Cheynet, S. Pokrant, F. D. Tichelaar, and J.-L. Rouvière, Crystal structure and band gap determination of HfO_2 thin films, J. Appl. Phys. **101**, 054101 (2007).

[4] X. Zhao and D. Vanderbilt, First-principles study of structural, vibrational, and lattice dielectric properties of hafnium oxide, Phys. Rev. B **65**, 233106 (2002).

[5] J. N. A. Matthews, Semiconductor industry switched to hafnium-based transistors, Phys. Today **61**(12), 25 (2008).

[6] F. Cardarelli, *Materials Handbook* (Springer, London, 2000).

[7] O. Ohtaka, H. Fukui, T. Kunisada, T. Fujisawa, K. Funakoshi, W. Utsumi, T. Irifune, K. Kuroda, and T. Kikegawa, Phase relations and volume changes of hafnia under high pressure and high temperature, J. Am. Ceram. Soc. **84**, 1369 (2001).

[8] T. S. Böscke, J. Müller, D. Bräuhaus, U. Schröder, and U. Böttger, Ferroelectricity in hafnium oxide thin films, Appl. Phys. Lett. **99**, 102903 (2011).

[9] X. Sang, E. D. Grimley, T. Schenk, U. Schroeder, and J. M. LeBeau, On the structural origins of ferroelectricity in HfO_2 thin films, Appl. Phys. Lett. **106**, 162905 (2015).

[10] M. H. Park, Y. H. Lee, H. J. Kim, Y. J. Kim, T. Moon, K. D. Kim, J. Müller, A. Kersch, U. Schroeder, T. Mikolajick, and C. S. Hwang, Ferroelectricity and antiferroelectricity of doped thin HfO_2-based films, Adv. Mater. **27**, 1811 (2015).

[11] D. W. McComb, Bonding and electronic structure in zirconia pseudopolymorphs investigated by electron energy-loss spectroscopy, Phys. Rev. B **54**, 7094 (1996).

[12] M. Launay, F. Boucher, and P. Moreau, Evidence of a rutile-phase characteristic peak in low-energy loss spectra, Phys. Rev. B **69**, 035101 (2004).

[13] J. Frandon, B. Brousseau, and F. Pradal, Electronic excitations in some transition metals and their oxides, Phys. Status Solidi B **98**, 379 (1980).

[14] M. P. Augustin, L. R. C. Fonseca, J. C. Hooker, and S. Stemmer, Scanning transmission electron microscopy of gate stacks with HfO_2 dielectrics and TiN electrodes, Appl. Phys. Lett. **87**, 121909 (2005).

[15] M. Couillard, M. Kociak, O. Stéphan, G. A. Botton, and C. Colliex, Multiple-interface coupling effects in local electron-energy-loss measurements of band gap energies, Phys. Rev. B. **76**, 165131 (2007).

[16] J. Park and M. Yang, Determination of complex dielectric functions at HfO_2/Si interface by using STEM-VEELS, Micron **40**, 365 (2009).

[17] S. C. Liou, M.-W. Chu, Y. J. Lee, M. Hong, J. Kwo, and C. H. Chen, Surface exciton polariton in monoclinic HfO_2: Electron energy-loss spectroscopy study, New J. Phys. **11**, 103009 (2009).

[18] C. Guedj, L. Hung, A. Zobelli, P. Blaise, F. Sottile, and V. Olevano, Evidence for anisotropic dielectric properties of monoclinic hafnia using valence electron energy-loss spectroscopy in high-resolution transmission electron microscopy and *ab initio* time-dependent density-functional theory, Appl. Phys. Lett. **105**, 222904 (2014).

[19] L. Hung, C. Guedj, N. Bernier, P. Blaise, V. Olevano, and F. Sottile, Interpretation of monoclinic hafnia valence electron energy-loss spectra by time-dependent density functional theory, Phys. Rev. B **93**, 165105 (2016).

[20] Y. Zhou, S. C. Liou, M.-T. Lee, C. J. Klingshirn, X. Ge, W. C. H. Kuo, and G. J. Shu, Investigation of anisotropic π plasmon induced by the intrinsic crystallographic defects in topological crystalline insulator material-tin-substitutional lead selenide ($Pb_{1-x}Sn_xSe$), Appl. Phys. Lett. **116**, 182108 (2020).

[21] R. F. Egerton, *Electron Energy-Loss Spectroscopy in the Electron Microscope*, 3rd ed. (Springer, Berlin, 2011).

[22] M. Stöger-Pollach, Optical properties and bandgaps from low loss EELS: Pitfalls and solutions, Micron **39**, 1092 (2008).

[23] S. C. Liou, V. P. Oleshko, W. C. H. Kuo, T. J. Yang, and G.-J. Shu, Investigation of the excitations of plasmons and surface exciton polaritons in monoclinic gadolinium sesquioxide by electron energy-loss spectroscopy and plasmon spectroscopic imaging, RSC Adv. **12**, 10345 (2022).

[24] J. P. R. Bolton and M. Chen, Electron energy loss in multilayered slabs, Ultramicroscopy **60**, 247 (1955).

[25] J. P. R. Bolton and M. Chen, Electron energy loss in multilayered slabs. 2. Parallel incidence, J. Phys.: Condens. Matter **7**, 3389 (1955).

[26] G. Kresse and J. Hafner, *Ab initio* molecular dynamics for liquid metals, Phys. Rev. B **47**, 558(R) (1993).

[27] G. Kresse and J. Hafner, *Ab initio* molecular dynamics for open-shell transition metals, Phys. Rev. B **48**, 13115 (1993).

[28] G. Kresse and J. Hafner, *Ab initio* molecular-dynamics simulation of the liquid-metal-amorphous-semiconductor transition in germanium, Phys. Rev. B **49**, 14251 (1994).

[29] J. P. Perdew and Y. Wang, Accurate and simple analytic representation of the electron-gas correlation energy, Phys. Rev. B **45**, 13244 (1992).

[30] J. P. Perdew, J. A. Chevary, S. H. Vosko, K. A. Jackson, M. R. Pederson, D. J. Singh, and C. Fiolhais, Atoms, molecules, solids and surfaces: Applications of the generalized gradient approximation for exchange and correlation, Phys. Rev. B **46**, 6671 (1992); **48**, 4978 (1993).

[31] P. E. Blöchl, Projector augmented-wave method, Phys. Rev. B **50**, 17953 (1994).

[32] G. Kresse and D. Joubert, From ultrasoft pseudopotentials to the projector augmented-wave method, Phys. Rev. B **59**, 1758 (1999).

[33] R. N. Patil and E. C. Subbarao, Axial thermal expansion of ZrO_2 and HfO_2 in the range room temperature to 1400 °C, J. Appl. Crystallogr. **2**, 281 (1969).

[34] S. Pathak, P. Das, T. Das, G. Mandal, B. Joseph, M. Sahu, S. D. Kaushik, and V. Siruguri, Crystal structure of monoclinic hafnia (HfO_2) revisited with synchrotron x-ray, neutron diffraction and first-principles calculations, Acta Crystallogr. Sect. C: Struct. Chem. **76**, 1034 (2020).

[35] G. D. Wilk and D. A. Muller, Correlation of annealing effects on local electronic structure and macroscopic electrical properties for HfO_2 deposited by atomic layer deposition, Appl. Phys. Lett. **83**, 3984 (2003).

[36] D. W. McComb, A. J. Craven, D. A. Hamilton, and M. MacKenzie, Probing local coordination environments in high-k materials for gate stack applications, Appl. Phys. Lett. **84**, 4523 (2004).

[37] M. P. Agustin, G. Bersuker, B. Foran, L. A. Boatner, and S. Stemmer, Scanning transmission electron microscopy investigations of interfacial layers in HfO_2 gate stacks, J. Appl. Phys. **100**, 024103 (2006).

[38] S. U. Sharath, S. Vogel, L. Molina-Luna, E. Hildebrandt, C. Wenger, J. Kurian, M. Duerrschnabel, T. Niermann, G. Niu, P. Calka, M. Lehmann, H.-J. Kleebe, T. Schroeder, and L. Alff, Control of switching modes and conductance quantization in oxygen engineered HfO_x based memristive devices, Adv. Funct. Mater. **27**, 1700432 (2017).

[39] J. H. Jang, H.-S. Jung, J. H. Kim, S. Y. Lee, C. S. Hwang, and K. Kim, Investigation of oxygen-related defects and the electrical properties of atomic layer deposited HfO_2 films using electron energy-loss spectroscopy, J. Appl. Phys. **109**, 023718 (2011).

[40] H. Raether, *Excitation of Plasmons and Interband Transitions by Electrons*, Springer Tracts in Modern Physics Vol. 88 (Springer-Verlag, Berlin, 1980).

[41] N. I. Medvedeva, V. P. Zhukov, M. Y. Khodos, and V. A. Gubanov, The electronic structure and cohesive energy of HfO_2, ZrO_2, TiO_2, and SnO_2 crystals, Phys. Status Solidi **160**, 517 (1990).

[42] T. V. Perevalov, V. A. Gritsenko, S. E. Erenburg, A. M. Badalyan, H. Wong, and C. W. Kim, Atomic and electronic structure of amorphous and crystalline hafnium oxide: X-ray photoelectron spectroscopy and density functional calculations, J. Appl. Phys. **101**, 053704 (2007).

[43] See Supplemental Material at http://link.aps.org/supplemental/10.1103/PhysRevMaterials.7.065201 for the figure showing the calculated relativistic *E*-*k* intensity maps for 50 nm thick m-HfO_2 slab with different impact parameters [Fig. S1(a)] and the experimental aloof beam low-loss STEM-EEL spectra acquired from the same impact parameter positions [Fig. S1(b)], which originated from Figs. 2(a) and 2(e), respectively, for comparison.

[44] J. Park, S. Heo, J.-G. Chung, H. Kim, H. Lee, K. Kim, and G.-S. Park, Bandgap measurement of thin dielectric films using monochromated STEM-EELS, Ultramicroscopy **109**, 1183 (2009).

[45] Q. Li, K. M. Koo, W. M. Lau, P. F. Lee, J. Y. Dai, Z. F. Hou, and X. G. Gong, Effects of Al addition on the native defects in hafnia, Appl. Phys. Lett. **88**, 182903 (2006).

[46] C. H. Chen, J. Silcox, and R. Vincent, Electron-energy losses in silicon: Bulk and surface plasmons and Čerenkov radiation, Phys. Rev. B **12**, 64 (1975).

[47] E. Z. Kröger, Berechnung der Energieverluste schneller Elektronen in dünnen Schichten mit Retardierung, Z. Phys. **216**, 115 (1968).

[48] K. A. Mkhoyan, T. Babinec, S. E. Maccagnano, E. J. Kirkland, and J. Silcox, Separation of bulk and surface-losses in low-loss EELS measurements in STEM, Ultramicroscopy **107**, 345 (2007).

[49] J. Tauc, *Amorphous and Liquid Semiconductors* (Plenum, New York, 1974).

[50] D. Muñoz Ramo, J. L. Gavartin, A. L. Shluger, and G. Bersuker, Spectroscopic properties of oxygen vacancies in monoclinic HfO_2 calculated with periodic and embedded cluster density functional theory, Phys. Rev. B **75**, 205336 (2007).

[51] S. Sayan, T. Emge, E. Garfunkel, X. Zhao, L. Wielunski, R. A. Bartynski, D. Vanderbilt, J. S. Suehle, S. Suzer, and M. Banaszak-Holl, Band alignment issue related to HfO_2/SiO_2/*p*-Si gate stacks, J. Appl. Phys. **96**, 7485 (2004).

[52] C. G. Fuentes, I. G. Mancheño, F. Balbás, C. Quirós, J. F. Trigo, F. Yubero, E. Elizalde, and J. M. Sanz, Dielectric properties of Ti, TiO_2, and TiN from 1.5 to 60 eV determined by reflection electron energy loss spectroscopy (REELS) and ellipsometry, Phys. Status Solidi A **175**, 429 (1999).

[53] L. K. Dash, F. Bruneval, V. Trinité, N. Vast, and L. Reining, Electronic excitations: *Ab initio* calculations of electronic spectra and application to zirconia ZrO_2, titania TiO_2 and cuprous oxide Cu_2O, Comput. Mater. Sci. **38**, 482 (2007).

[54] L. K. Dash, N. Vast, P. Baranek, M.-C. Cheynet, and L. Reining, Electronic structure and electron energy-loss spectroscopy of ZrO_2 zirconia, Phys. Rev. B **70**, 245116 (2004).

[55] S. C. Liou, M.-W. Chu, R. Sankar, F.-T. Huang, G. J. Shu, C. C. Chou, and C. H. Chen, Plasmons dispersion and nonvertical interband transitions in single crystal Bi_2Se_3 investigated by electron energy-loss spectroscopy, Phys. Rev. B **87**, 085126 (2013).